Energy Advances

ROYAL SOCIETY OF CHEMISTRY

PAPER

View Article Online
View Journal | View Issue

Check for updates

Cite this: *Energy Adv.*, 2023, 2, 1409

Structural and kinetic adjustments of Zr-based high-entropy alloys with Laves phases by substitution of Mg element

Fuhu Yin,†[a] Yu Chang,†[b] Tingzhi Si,*[a] Jing Chen,[b] Hai-Wen Li,[c] Yongtao Li*[ad] and Qingan Zhang[a]

Received 31st May 2023,
Accepted 19th July 2023

DOI: 10.1039/d3ya00243h

rsc.li/energy-advances

Exploration of high-entropy alloys for hydrogen storage has recently attracted attention owing to their serious defects, high-entropy induced reduction of thermodynamic stability and abundant raw metal elements. In this study, new Zr-based high-entropy alloys with Laves phases were designed where their structure and hydrogen storage properties were adjusted by introducing Mg element. The results show that the addition of Mg element makes the crystal structure of $Zr_2MgV_{2-x}Fe_xCrNi$ (x = 0 and 1) alloys change from AB_2 type to A_3B_4 type structure, which further leads to the improvement of their hydrogen storage capacity and hydrogen sorption kinetics. The Zr_2MgV_2CrNi and $Zr_2MgVFeCrNi$ high-entropy alloys can rapidly absorb 0.8 wt% (0.43 H/M) and 0.9 wt% (0.48 H/M) hydrogen at room temperature, respectively, three times higher than those of the Zr-based alloys without Mg-substitution. And more importantly, the absorbed hydrogen of Zr_2MgV_2CrNi and $Zr_2MgVFeCrNi$ high-entropy alloys can be partially released at room temperature with distinct desorption processes. These capacity and kinetic enhancements should be related to the higher lattice parameters, lower electron concentration, severe lattice distortion and smaller average valence electron concentration (VEC) of those alloys. The development of Mg-containing Zr-based high-entropy alloys with Laves phases provides a new idea for the design of new hydrogen storage materials.

Open Access Article. Published on 19 de juliol 2023. Downloaded on 31/1/2026 14:14:17.
This article is licensed under a Creative Commons Attribution-NonCommercial 3.0 Unported Licence.

1. Introduction

The serious energy and environmental crisis propel people to develop and utilize clean energy. In that regard, hydrogen as an energy carrier is considered a potential energy solution owing to its abundant source, cleanliness, renewability and high energy density; however, its storage is still a challenge.[1–3] Compared with high-pressure gaseous hydrogen storage and low-temperature liquefied hydrogen storage, solid-state hydrogen storage has been widely studied owing to its high energy density and safety.[4,5] To date, a variety of solid hydrogen storage materials have been proposed and studied, such as complex hydrides that can store hydrogen at near room temperature,[6–8] Mg-based alloys with high hydrogen storage capacity[9–12] and intermetallic compounds that can reversibly store hydrogen at room temperature.[13–15] However, none of them satisfies all the requirements for a hydrogen storage material in practical applications. Thus, it is very important to explore new hydrogen storage alloys.

Recently, high-entropy alloys (HEAs), which contain five or more elements in relatively high concentrations (5–35 at%) and have a random state of coordination entropy greater than 1.5 R, have received significant attention for hydrogen storage applications.[16–18] This is because under the influence of the cocktail effect, all the principal components will affect the performance of the alloy. Due to the diversity of element selection and the controllability of element ratio, it is possible to prepare high-entropy alloys with good properties for hydrogen storage applications.[18–20]

Owing to the above-mentioned advantages, some high-entropy alloys for hydrogen storage have been designed. Among them, the intermetallic high-entropy alloys containing Laves phases have attracted much attention owing to their high hydrogen storage capacity and good low-temperature reversible hydrogen storage performance. In recent years, several Laves phase high-entropy alloys have been studied but their reversibility is poor. For example, the hydrogen absorption capacity of the CoFeMnTiVZr high-entropy alloy is 1.4 wt% but its reversible hydrogen storage capacity is only 0.7 wt%.[21] The hydrogen

[a] School of Materials Science and Engineering, Anhui University of Technology, Maanshan 243002, China. E-mail: liyongtao@ahut.edu.cn, tzsiahut@163.com; Tel: +86-555-2311 570
[b] Institute of Nuclear and New Energy Technology, Tsinghua University, Beijing, 100084, China
[c] Hefei General Machinery Research Institute, Hefei 230031, China
[d] Key Laboratory of Green Fabrication and Surface Technology of Advanced Metal Materials of Ministry of Education, Anhui University of Technology, Maanshan 243002, China
† These authors contributed equally to this work.

© 2023 The Author(s). Published by the Royal Society of Chemistry

Open Access Article. Published on 19 de juliol 2023. Downloaded on 31/1/2026 14:14:17.
This article is licensed under a Creative Commons Attribution-NonCommercial 3.0 Unported Licence.

absorption capacity of the LaNiFeVMn high-entropy alloy is 0.82 wt%, but its reversible hydrogen storage capacity is only 0.2 wt%.[22] In this regard, Edalati *et al.*[23] designed a TiZrCrMnFeNi high-entropy alloy with C14 Laves phase. They show that a valence electron concentration (VEC) of 6.4 is associated with a fast reversible hydrogen capacity of 1.7 wt% at room temperature without the activation process. Unfortunately, the cycling performance of the alloy has not been tested. On this basis, Mohammadi *et al.*[24] used first-principles calculations to design AB_2-type Laves phase $Ti_xZr_{2-x}CrMnFeNi$ (x = 0.4–1.6) alloys with a valence electron concentration of 6.4 and low hydrogen binding energies (negative values close to −0.1 eV), which reversibly absorb and desorb hydrogen at room temperature (298 K) with fast kinetics. Among them, the hydrogen storage capacity of the $Ti_{0.4}Zr_{1.6}CrMnFeNi$ alloy is almost unchanged at 1.6 wt% after 1000 cycles at 3.7 MPa and 298 K. This not only shows that the alloy has excellent cycling properties, but also implies that the concept of binding energy engineering can be used to adjust the temperature and pressure of hydrogen storage in high-entropy alloys to adapt to environmental conditions. After that, Chen *et al.*[25] designed a TiZrFeMnCrV high-entropy alloy with single C14 Laves phase, and its capacity remained stable at about 1.76 wt% after 50 cycles.

However, these alloys do not show better hydrogen storage performance than traditional intermetallic compounds, which may be related to the large number of transition metal elements in the alloys and the composition system and crystal structure of high-entropy alloys. In this regard, Floriano *et al.*[26] reported the A_3B_2-type TiZrNbFeNi and AB-type $Ti_{20}Zr_{20}Nb_5Fe_{40}Ni_{15}$ high-entropy alloys, and found that the non-equiatomic alloys have a larger reversible hydrogen storage capacity, which is related to the larger valence electron concentration. After that, the research group[27] reported an A_3B_2 type TiZrNbCrFe high-entropy alloy that can reversibly absorb and release 1.9 wt% hydrogen at 473 K. Recently, Andrade *et al.*[28] also reported an AB-type TiZrNbFeCrNi high-entropy alloy that can reversibly absorb 1.1 wt% hydrogen at 473 K. Therefore, to have higher H/M values at room or moderate temperatures, new systems with different A/B ratios should be designed. In addition, the use of light-weight alloying elements is also the key to efficient hydrogen storage. In this regard, Ma *et al.*[29] reported $ZrTiVAl_{1-x}Fe_x$ high-entropy alloys. Due to the severe lattice distortion and friable HCP interdendritic phase, these alloys exhibited rapid hydrogen chemisorption kinetics even at room temperature. In addition, the study also shows that the increase of VEC will lead to the decrease of the stability of alloy hydrides. However, although the addition of the light element Mg to the intermetallic high-entropy alloy can also reduce the density of the alloy and has the possibility of further improving the hydrogen storage capacity, there are few studies on magnesium-containing Lave-phase high-entropy alloys for hydrogen storage. This may be related to the preparation of Mg Laves phase hydrogen storage high entropy alloys: due to the large difference in melting and boiling points between Mg and transition metal elements such as Zr and V, this makes it impossible to accurately prepare Mg Laves phase hydrogen storage high entropy alloys using conventional melting methods, and the production is unsafe. In addition, the use of mechanical alloying to prepare Mg-containing high-entropy alloys not only requires a long ball milling time, which leads to the risk of contamination and oxidation of the alloy, but also makes it difficult to prepare high-purity Laves-phase Mg-hydrogen storage high-entropy alloys, which leads to deterioration of the material properties.

In this study, $Zr_2MgV_{2-x}Fe_xCrNi$ (x = 0 and 1) was first prepared by a combination of melting, ball milling and sintering. The effects of Mg addition on the microstructure and hydrogen storage properties of Zr-based Laves phase high-entropy alloys were studied in detail, and the hydrogen storage mechanism of these two Mg-containing Laves phase high-entropy alloys was also revealed.

2. Experimental

2.1 High-entropy alloy fabrication

First, the $Zr_2V_yFe_{1-y}CrNi$ (x = 0 and 1) master alloys prepared by arc melting were crushed into 200-mesh powders in a glove box under a dry argon atmosphere. Following that, the stoichiometric amounts of the as-prepared master alloy and commercial Mg were mixed manually for 5 min in the glove box and subsequently introduced into a stainless steel vial for ball-milling. An extra 20 wt% Mg was added to compensate for the loss of Mg for the following heat-treatment. The milling was performed using a QM-1SP planetary mill under argon (0.2 MPa) at a rotation speed of 400 rpm for 5 h. Stainless steel vials (250 ml in volume) and balls (10 mm in diameter) were used. The weight of the powder was 4 g and the ball-to-powder weight ratio was 40 : 1. In order to reduce Mg vaporization and ensure composition homogeneity, the ball-milled samples were pressed into pellets and then sintered at 450, 750 and 850 °C for 3 h, 3 h and 4 h under an argon atmosphere (about 0.6 MPa). Afterwards, the alloys were quenched to room temperature.

2.2 Structure characterization

X-ray diffraction (XRD) measurements were carried out by using a Rigaku Miniflex diffractometer with Cu K_a radiation at 40 kV and 15 mA. Meanwhile, the XRD pattern of a Si standard reference material was also measured for instrumental profile calibration. In order to determine the phase components and structural parameters of the samples, the XRD profiles were refined with the Rietveld method using the program package RIETAN-2000.[30] For the Rietveld refinements, a pseudo-Voigt function with a Gaussian part and a Lorentzian part was used for expressing peak profiles. The particle morphology of the samples was analyzed using a scanning electron microscope (SEM, Tescan MIRA 3 XMU) equipped with an energy-dispersive X-ray spectrometer (EDS), where the scanning electron microscope was operated at 10–20 KV. The microstructure observation was conducted using a JEM2100 transmission electron microscope.

2.3 Hydrogen storage tests

The hydrogen storage performances were measured using a manual Sieverts-type apparatus. Before each test, the samples

© 2023 The Author(s). Published by the Royal Society of Chemistry

Open Access Article. Published on 19 de juliol 2023. Downloaded on 31/1/2026 14:14:17.
This article is licensed under a Creative Commons Attribution-NonCommercial 3.0 Unported Licence.

need to be activated. 0.15 g powder samples were placed in the reaction vessel. After cleaning and leak testing the device, the reaction vessel was heated to 350 °C in a resistance furnace and then charged with 3.5 MPa hydrogen pressure to allow the sample to fully absorb hydrogen for 1 h. The samples were then evacuated for 1 h to fully release the hydrogen. The activation was completed by letting the samples subject to three hydriding/dehydriding cycles. The activated samples were cooled to room temperature and then the furnace was ramped up from room temperature at 5 °C min^{-1} and the room temperature, sample temperature and pressure were recorded until the pressure was constant. The sample temperature and pressure were recorded until the pressure was constant. The hydrogen release capacity of the samples was then calculated using the template to produce the sample warming and release curve. The samples were then cooled to 303 K and charged with a hydrogen pressure of 3 MPa to allow the samples to fully absorb hydrogen, then the sample temperature and pressure were recorded and the template was used to calculate the hydrogen absorption capacity of the samples to produce a constant temperature hydrogen absorption curve. Similarly, the temperature of the activated samples was maintained at 303 K, 373 K, 473 K and 523 K. The sample was then evacuated to 0.001 MPa to allow full hydrogen release and the changes in time, temperature and pressure were recorded and the hydrogen release capacity was calculated using the template to produce a constant temperature release curve.

3. Results

3.1. Structural and morphological features of $Zr_2V_yFe_{1-y}CrNi$ alloys by introduction of Mg element

Fig. 1 shows the Rietveld refinement of the XRD patterns for the $Zr_2Mg_xV_yFe_{1-y}CrNi$ (x = 0 and 1, and y = 0 and 1) high-entropy alloys. It is found that both the Zr_2V_2CrNi precursor and the Zr_2MgV_2CrNi high-entropy alloy contain C14 Laves phase and C15 Laves phase, while the $Zr_2VFeCrNi$ precursor sample and the $Zr_2MgVFeCrNi$ high-entropy alloy only contain single C14 Laves phase. The structural parameters and phase fractions of $Zr_2Mg_xV_yFe_{1-y}CrNi$ (x = 0 and 1, and y = 0 and 1) high-entropy alloys refined by the Rietveld analysis are further listed in Table 1. It can be seen that the content of C14 Laves phase in the Zr_2V_2CrNi precursor sample and Zr_2MgV_2CrNi high-entropy alloy is close to 90 wt%. This clearly indicates that the high purity Laves phase type high-entropy alloy containing magnesium can be prepared by a combination of melting, ball milling and sintering steps. In addition, the addition of Mg increases slightly the lattice parameters of the alloy, which would facilitate the rapid transfer of hydrogen atoms.

The microstructural features of Zr_2MgV_2CrNi and $Zr_2MgVFeCrNi$ high-entropy alloys are further studied by using the SEM technique and the corresponding mapping images are also presented in Fig. 2 and 3. It can be found that all the particles of the high-entropy alloys are lumpy-like with a size of about 10–100 μm. In addition, the elemental mapping shows that the elements Zr, Mg, V, Cr and Ni in the Zr_2MgV_2CrNi alloy and Zr, Mg, V, Fe, Cr and Ni in the $Zr_2MgVFeCrNi$ alloy are uniformly distributed within the alloys.

In order to further reveal the microstructure of the Zr_2MgV_2CrNi high-entropy alloy, TEM and HRTEM techniques were employed. Fig. 4(a) shows the TEM image of the Zr_2MgV_2CrNi sample. The SAED of the corresponding particle (see Fig. 4(b)) displays a set of ordered arrays of diffraction points and diffraction rings, which can be identified as C14 Laves phase and C15 Laves phase, agreeing well with the XRD results (Fig. 1(c)). The HRTEM image in Fig. 4(c) further confirms the existence of these two phases, where the d-spacing of 0.300 and 0.204 nm is observed, corresponding to

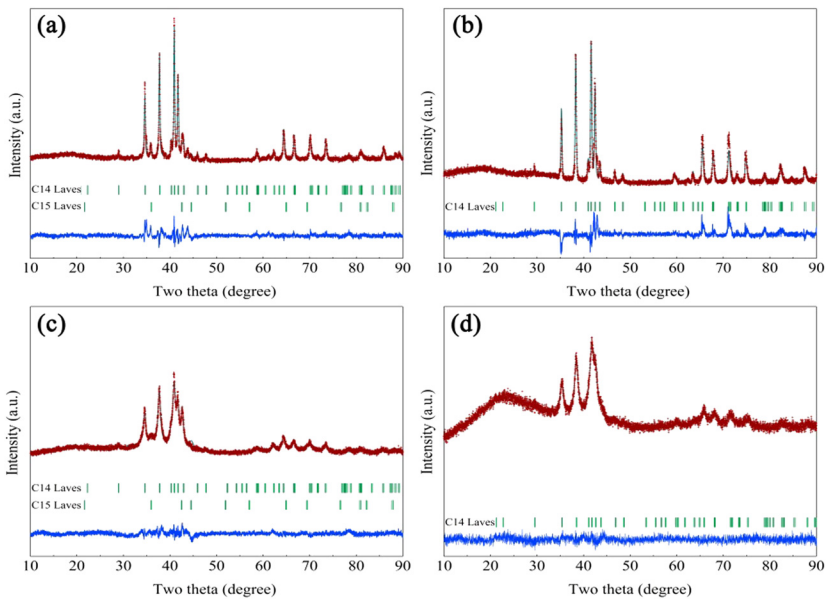

Fig. 1 Rietveld refinements of the XRD patterns for (a) Zr_2V_2CrNi, (b) $Zr_2VFeCrNi$, (c) Zr_2MgV_2CrNi and (d) $Zr_2MgVFeCrNi$ high-entropy alloys.

Open Access Article. Published on 19 de juliol 2023. Downloaded on 31/1/2026 14:14:17.
This article is licensed under a Creative Commons Attribution-NonCommercial 3.0 Unported Licence.

Table 1 Structural parameters and phase fractions of the Zr_2V_2CrNi, $Zr_2VFeCrNi$, Zr_2MgV_2CrNi and $Zr_2MgVFeCrNi$ high-entropy alloys

Sample	Phase	Lattice parameters (Å)		Abundance (wt%)
		a	*c*	
Zr_2V_2CrNi (R_{WP} = 6.94%; S = 3.17)	C14 Laves	5.0765(2)	8.2744(2)	90
	C15 Laves	6.9256(4)		10
$Zr_2VFeCrNi$ (R_{WP} = 9.12%; S = 3.73)	C14 Laves	4.9987(2)	8.1744(1)	100
Zr_2MgV_2CrNi (R_{WP} = 5.38%; S = 2.80)	C14 Laves	5.0802(7)	8.2967(1)	88
	C15 Laves	6.9340(5)		12
$Zr_2MgVFeCrNi$ (R_{WP} = 5.25%; S = 2.73)	C14 Laves	5.0031(1)	8.1748(1)	100

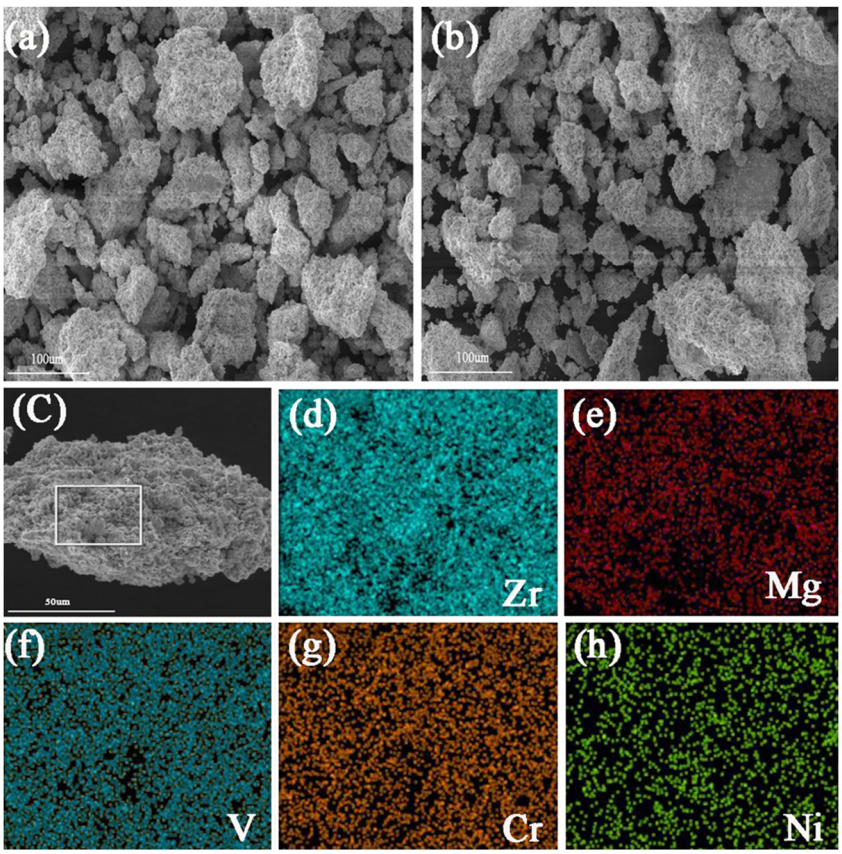

Fig. 2 SEM images (a)–(c) and EDS mappings (d)–(h) of the Zr_2MgV_2CrNi high-entropy alloys.

the (102) and (222) planes for C14 and C15 Laves phases, respectively.

3.2. Enhanced hydrogen de-/absorption behaviours of $Zr_2V_yFe_{1-y}CrNi$ by doping Mg element

Fig. 5 shows the hydrogen absorption kinetic curves of $Zr_2Mg_xV_{2-y}Fe_yCrNi$ (x = 0 and 1, and y = 0 and 1) high-entropy alloys at 303 K under 4 MPa hydrogen pressure. It can be seen that the four alloys have good hydrogen absorption kinetics at room temperature, the hydrogen storage capacities of Zr_2V_2CrNi, $Zr_2VFeCrNi$, Zr_2MgV_2CrNi and $Zr_2MgV_2FeCrNi$ are 0.3, 0.55, 0.8 and 0.9 wt%, respectively, and their hydrogen-to-metal ratios (H/M) are 0.17, 0.32, 0.43 and 0.48, respectively, indicating that the addition of Mg increases the hydrogen storage capacity of high-entropy alloys to a certain extent,and this should be attributed to the structural transformation and the decrease of alloy density caused by the addition of Mg element. In addition, the hydrogen storage capacity of high-entropy alloys is improved after Fe element replaces V element, which may be related to the increase of the content of C14 Laves phase with relatively large hydrogen storage capacity in the alloy.

Fig. 6 shows hydrogen desorption kinetic behaviours of $Zr_2Mg_xV_{2-y}Fe_yCrNi$ (x = 0 and 1, and y = 0 and 1) high-entropy alloys at different temperatures. It can be seen that all high-entropy alloys can dehydrogenate at room temperature, and more hydrogen is released with the increasing desorption temperature. In addition, Zr_2V_2CrNi and $Zr_2VFeCrNi$ alloys can be completely dehydrogenated at 373 K, while Zr_2MgV_2CrNi and $Zr_2MgVFeCrNi$ alloys can be completely dehydrogenated

© 2023 The Author(s). Published by the Royal Society of Chemistry

Open Access Article. Published on 19 de juliol 2023. Downloaded on 31/1/2026 14:14:17.
This article is licensed under a Creative Commons Attribution-NonCommercial 3.0 Unported Licence.

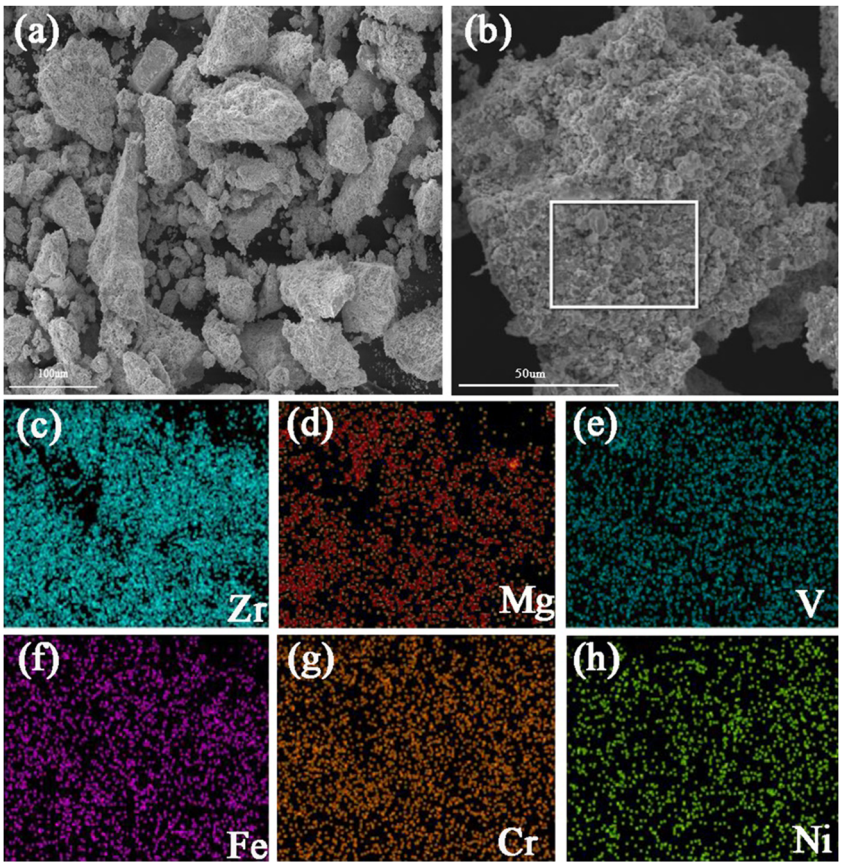

Fig. 3 SEM images (a) and (b) and EDS mappings (c)–(h) of the $Zr_2MgVFeCrNi$ high-entropy alloys.

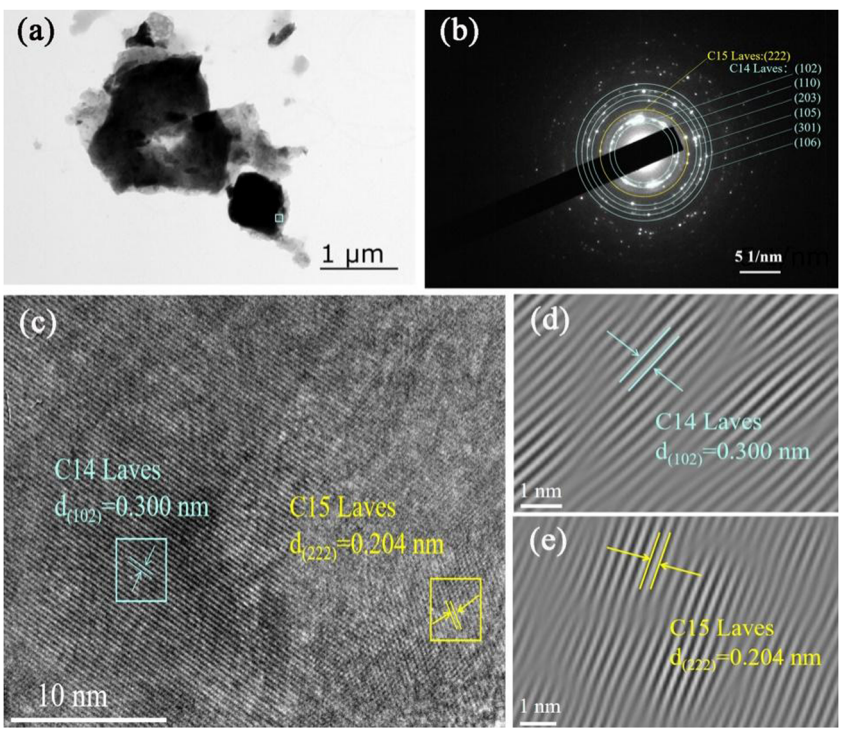

Fig. 4 Microstructural characterization of the Zr_2MgV_2CrNi sample: (a) TEM image, and (b) corresponding SAED patterns; (c) HRTEM image and the corresponding IFFT images (d) and (e) of C14 and C15 Laves phases.

Open Access Article. Published on 19 de juliol 2023. Downloaded on 31/1/2026 14:14:17.
This article is licensed under a Creative Commons Attribution-NonCommercial 3.0 Unported Licence.

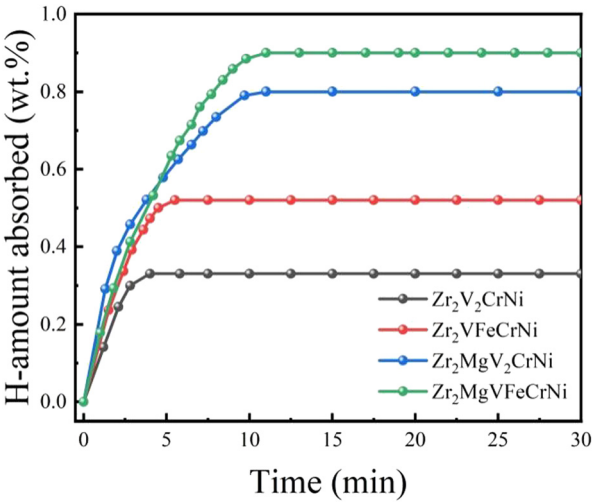

Fig. 5 Hydrogen absorption kinetics curves of $Zr_2Mg_xV_{2-y}Fe_yCrNi$ (x = 0 and 1, and y = 0 and 1) high-entropy alloys at 303 K.

only at 523 K, indicating that the addition of Mg has an adverse effect on the stability of the alloy hydride.

3.3. Hydrogen de-/absorption mechanisms of $Zr_2MgV_{2-x}Fe_xCrNi$ high-entropy alloys

In order to analyse the hydrogen absorption and desorption mechanism of $Zr_2MgV_{2-x}Fe_xCrNi$ high-entropy alloys, the TPD test was used for these two alloys, and the XRD patterns of the alloys at each stage were analysed, and the results are shown in Fig. 7. It can be seen that after complete hydrogen absorption, hydrogen absorption occurs in both Laves phases in the Zr_2MgV_2CrNi high-entropy alloy, resulting in a shift of its X-ray diffraction peak to a lower angle, and that hydride also contains ZrH_2. In addition, the alloy began to dehydrogenate at about 30 °C, and the first stage of dehydrogenation was completed at about 244 °C. At this stage, the hydrogen desorption was relatively slow, and a total of about 0.44 wt% was dehydrogenated. After that, the alloy completed the second stage of dehydrogenation at about 285 °C, and this also means that the hydride has been completely dehydrogenated at this time. This stage of dehydrogenation was faster, which may be related to the higher temperature of this stage. It can be seen from the XRD pattern that both Laves phases in the alloy are dehydrogenated in the first stage, and the C15 Laves phase has been completely dehydrogenated after the first stage, which makes only the C14 Laves phase dehydrogenate in the second stage. In addition, the maximum dehydrogenation capacity of the alloy is about 0.7 wt%, which was less than its hydrogenation capacity, indicating that the alloy could not completely dehydrogenate, which was related to the formation of ZrH_2 during the hydrogenation process.

In addition, it can be seen from Fig. 7 that the C14 Laves phase of the $Zr_2MgVFeCrNi$ high-entropy alloy shifted toward the lower-angle during hydrogen absorption, and began to dehydrogenate at about 30 °C, and completely desorbed at about 282 °C. At this time, the C14 Laves phase returned to its original position, indicating that the alloy can completely reversibly absorb and desorb hydrogen, and the maximum hydrogen storage capacity is about 0.9 wt%. In summary, the final

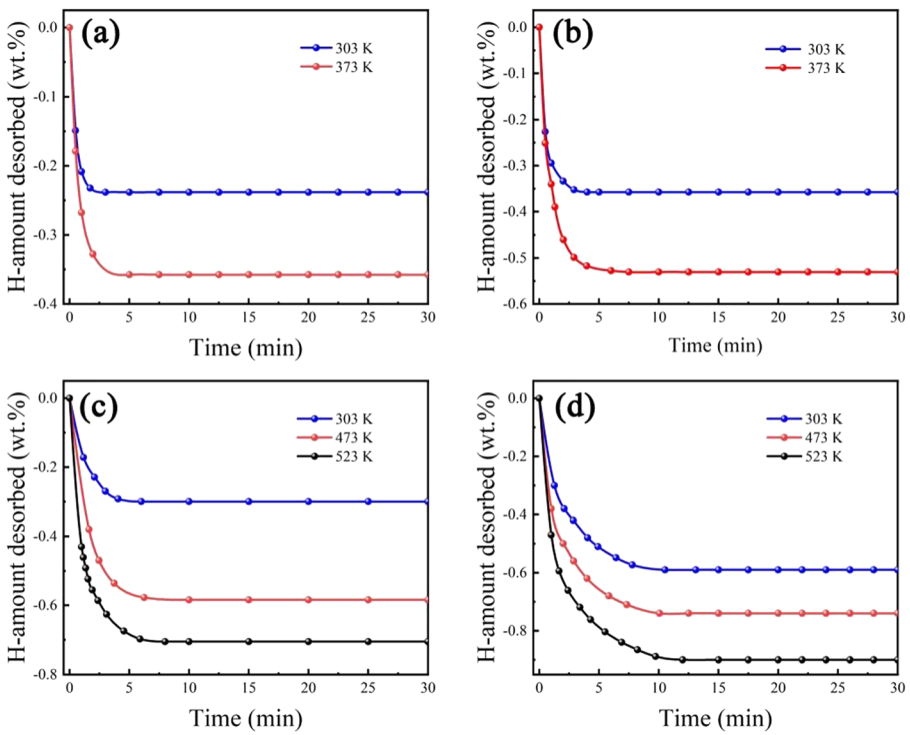

Fig. 6 Hydrogen desorption kinetic curves of (a) Zr_2V_2CrNi, (b) $Zr_2VFeCrNi$, (c) Zr_2MgV_2CrNi and (d) $Zr_2MgVFeCrNi$ high-entropy alloys at different temperatures.

© 2023 The Author(s). Published by the Royal Society of Chemistry

Open Access Article. Published on 19 de juliol 2023. Downloaded on 31/1/2026 14:14:17.
This article is licensed under a Creative Commons Attribution-NonCommercial 3.0 Unported Licence.

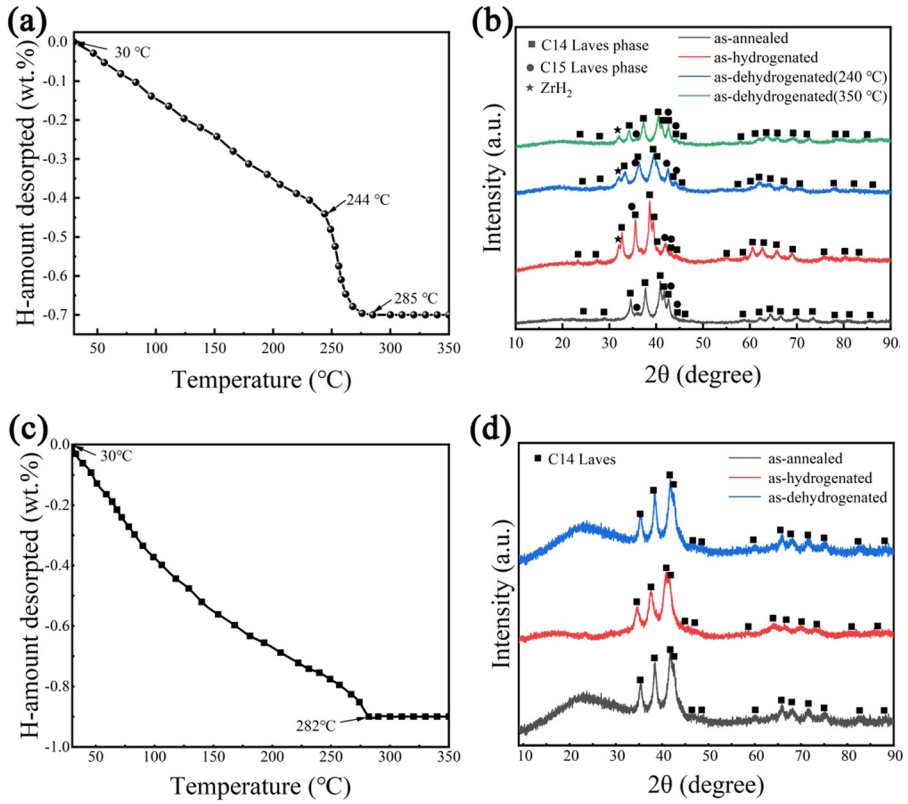

Fig. 7 TPD profile of (a) Zr_2MgV_2CrNi and (c) $Zr_2MgVFeCrNi$ high-entropy alloys at a heating rate of 5 °C min^{-1}, as well as their XRD patterns for (b) Zr_2MgV_2CrNi and (d) $Zr_2MgVFeCrNi$ high-entropy alloys at different states.

hydrogen release temperature of both high-entropy alloys is around 280 °C. This indicates that the substitution of Fe element basically does not improve the thermodynamic properties of the alloy, which is related to the fact that both alloys contain a large amount of V element and the structure of the alloy, because too much V element is not conducive to the hydrogen release of the alloy, and there is an excess of A-side atoms in this alloy, which makes some A-side atoms occupy the position of the B-side atoms, thus leading to an increase in the cell volume of the alloy. Eventually, the pressure of the hydrogen release plateau of these alloys decreases, which is not favorable for the release of hydrogen.[22,28]

4. Discussion

In this study, the phase structure and hydrogen storage properties of $Zr_2Mg_xV_{2-y}Fe_yCrNi$ high-entropy alloys are affected by the parameters of δ_r (atomic size mismatch), $\Delta\chi_{Allen}$ (Allen electronegativity difference), VEC (average valence electron concentration) and e/a (electron concentration).[29,31–35]

$$\delta_r = 100\%\sqrt{c_i(1 - r_i/\bar{r})^2} \quad (1)$$

$$\Delta\chi_{Allen} = 100\%\sqrt{\sum c_i(1 - \chi_{iAllen}/\chi_\alpha)^2} \quad (2)$$

$$VEC = \Sigma c_i VEC_i \quad (3)$$

$$e/a = Z_1C_1 + Z_2C_2 + \ldots + Z_mZ_m \quad (4)$$

here r_i, χ_i and VEC_i are the atomic radius, electronegativity and valence electron concentration of element i; c_i is the atomic fraction of atom i; $\bar{r}$ ($=\Sigma c_i r_i$) and χ_α ($=\Sigma c_i\chi_i$) are the average atomic radius and electronegativity. Z_i ($i = 1 - m$) is the valence electron number of group i, and C_i is the atomic percentage of group I ($C_1 + C_2 + \ldots + C_m = 1$). For group VIII, the number of valence electrons is zero ($Z = 0$), and for other groups, the number of valence electrons is equal to the group number in the periodic table (Z = N). Table 2 shows the atomic radii, Allen electronegativity, VEC and e/a values of different elements.[29]

(i) In the previous study,[33] the criteria for alloys containing the Laves phase were obtained as $\delta_r > 5.0\%$ and $\Delta\chi_{Allen} > 7.0\%$, which is consistent with the results of this study.

(ii) The addition of Mg to the Zr-based Laves phase high-entropy alloy will lead to the decrease of the VEC value, and a larger VEC destabilizes the hydrides,[34] which makes the dehydrogenation temperature of $Zr_2MgV_{2-x}Fe_xCrNi$ hydride higher

Table 2 The δ_r, $\Delta\chi_{Allen}$, VEC and e/a parameters calculated for the $Zr_2Mg_xV_{2-y}Fe_yCrNi$ (x = 0 and 1, and y = 0 and 1) high-entropy alloys

Alloy	δ_r/%	$\Delta\chi_{Allen}$/%	VEC	e/a
Zr_2V_2CrNi	10.77	15.17	5.7	4
$Zr_2VFeCrNi$	11.18	13.80	6.2	3.2
Zr_2MgV_2CrNi	10.96	14.89	5.1	3.7
$Zr_2MgVFeCrNi$	11.48	14.78	5.6	3

Open Access Article. Published on 19 de juliol 2023. Downloaded on 31/1/2026 14:14:17.
This article is licensed under a Creative Commons Attribution-NonCommercial 3.0 Unported Licence.

than that of $Zr_2V_{2-x}Fe_xCrNi$ hydride. However, the final hydrogen release temperatures of these four high-entropy alloys are still high, which may be related to factors such as the VEC parameter in the alloys not yet reaching 6.4 and the large amount of elemental *V* in the alloys.[23,24]

(iii) In general, the larger the lattice parameters of the alloy, the higher the hydrogen storage capacity. However, in this study, the $Zr_2MgVFeCrNi$ high-entropy alloy with smaller lattice parameters has the highest hydrogen storage capacity, which is related to the VEC, *e*/*a* and alloy structure. Compared with the Zr_2MgV_2CrNi high-entropy alloy, the $Zr_2MgVFeCrNi$ high-entropy alloy contains only C14 Laves phase with relatively high hydrogen storage capacity, and its electron concentration is relatively low. According to Wagner's[36] theory, the higher electron concentration would result in the lower hydrogen absorption capacity, because more outer electrons of the alloy would exert stronger repulsive interaction to the hydrogen atoms, thus hindering the hydrogen atoms into the lattice, so the hydrogen storage capacity of the $Zr_2MgVFeCrNi$ high-entropy alloy is relatively high. Compared with the $Zr_2VFeCrNi$ high-entropy alloy, the Zr_2MgV_2CrNi high-entropy alloy not only has larger lattice parameters and smaller VEC and *e*/*a*, but also contains a light element Mg. Since a larger average valence electron concentration destabilizes the hydride, eventually this destabilization leads to a reduction in the maximum hydrogen storage capacity.[34] In addition, the addition of Mg not only reduces the density of the alloy, but also makes the alloy change from AB_2 type structure to A_3B_4 type structure, which leads to more defects in the alloy, and makes the position occupied by the B-side atoms in the alloy appear vacant. At the same time, some A-side atoms occupy the position of the B-side atoms, which leads to the increase of the cell volume of the alloy, and finally improves the hydrogen storage capacity and hydrogen absorption kinetics of the alloy.[37,38] Therefore, among the four alloys, the $Zr_2MgVFeCrNi$ high-entropy alloy has the highest hydrogen storage capacity. However, the hydrogen storage capacity of these four high-entropy alloys is low, which may be related to factors such as the structure of the alloys, the high content of transition group metal elements, and the larger *e*/*a* and VEC in the alloys.[34,36]

(iv) In this study, the four high-entropy alloys have good hydrogen absorption and desorption kinetics, which is related to lattice parameters, defects, electron concentration and alloy structure. Because the high-entropy alloy is composed of a variety of elements, the difference in atomic radius and electronegativity makes the alloy have more defects such as lattice distortion, dislocation and strain, and weaken the corresponding bond energy, which is more conducive to the diffusion, dissociation and recombination of hydrogen atoms.[25,29] Compared with the $Zr_2V_{2-x}Fe_xCrNi$ high-entropy alloy, the $Zr_2MgV_{2-x}Fe_xCrNi$ high-entropy alloy has better kinetic properties, which can be attributed to the fact that both alloys are under-stoichiometric alloys, and have higher lattice constants and smaller electron concentration, resulting in a larger tetrahedral gap of the alloy, which is more conducive to hydrogen absorption and desorption of the alloy.[35–38]

Table 3 compares the high entropy alloys in this study with some high entropy alloys. Although the hydrogen storage capacity of the high-entropy alloys in this study is lower than that of some Laves-phase high-entropy alloys,[25,39] the successful introduction of Mg element in this study resulted in the transformation of the high-entropy alloys from AB_2-type to A_3B_4-type structures, as well as the reduction of the VEC of the alloys, which improved the hydrogen storage capacity and kinetic properties of the alloys and demonstrated that A_3B_4-type Laves-phase high-entropy alloys can be designed to achieve high reversible hydrogen storage at moderate temperature. This provides insight into the design and performance improvement of new high-entropy alloys. Furthermore, the Mg-containing HEAs studied by predecessors are mainly composed of BCC/FCC phases, and generally have a high dehydrogenation temperature.[40,41] However, the high-entropy alloy in this study has a pure Laves phase and outstanding reversible hydrogen storage at room temperature, which indicates that the presence of the Laves phase is beneficial for the development of Mg-containing high-entropy alloys with excellent low-temperature reversibility.

Table 3 Comparison of the hydrogen storage properties of this study with those of some high entropy alloys[25,39–41]

HEAs	Phase	Storage capacity (wt%)	Start/end dehydrogenation temperature (K)
TiZrFeMnCrV	C14 Laves	1.8	323/773
TiVZrNbFe	C14 Laves (major)	1.65	303/641
MgAlTiFeNi	BCC	1.0	558/598
$Mg_{12}Al_{11}Ti_{33}$-$Mn_{11}Nb_{33}$	BCC	1.75	573/793
Zr_2MgV_2CrNi	C14 Laves (major)	0.8	303/558
$Zr_2MgVFeCrNi$	C14 Laves	0.9	303/555

5. Conclusions

In this study, novel $Zr_2Mg_xV_{2-y}Fe_yCrNi$ (x = 0 and 1, and y = 0 and 1) high-entropy alloys were successfully prepared by three steps and their structure and hydrogen storage properties were studied in detail. It can be demonstrated that the Zr_2MgV_2CrNi high-entropy alloy is composed of C14 Laves phase (88 wt%) and C15 Laves phase (12 wt%), while the $Zr_2MgVFeCrNi$ high-entropy alloy contains only a C14 Laves single phase structure. The $Zr_2MgVFeCrNi$ alloy delivers a maximum hydrogen storage capacity of about 0.9 wt% (0.48 H/M) at room temperature and better kinetics. The dehydrogenation process of the Zr_2MgV_2CrNi high-entropy alloy includes two distinct steps of C14 and C15 phases, while the hydrogen absorption and desorption of the $Zr_2MgVFeCrNi$ alloy occurs only through the volume expansion and contraction of the C14 Laves phase. The improvements of hydrogen absorption capacity and kinetics of $Zr_2V_{2-x}Fe_xCrNi$ alloys should be ascribed to the structural transformation and the decrease of alloy VEC induced by the addition of Mg element. These obtained results

© 2023 The Author(s). Published by the Royal Society of Chemistry

Open Access Article. Published on 19 de juliol 2023. Downloaded on 31/1/2026 14:14:17.
This article is licensed under a Creative Commons Attribution-NonCommercial 3.0 Unported Licence.

would provide insight into the design of new high-entropy alloys and their property improvements.

Author contributions

Fuhu Yin and Yu Chang: conceptualization, data curation, formal analysis, investigation, writing–original draft; Tingzhi Si: conceptualization, funding acquisition, supervision, writing–review & editing; Jing Chen: writing–review & editing; Hai-Wen Li: review & editing; Yongtao Li: conceptualization, visualization, funding acquisition, writing–review & editing; Qingan Zhang: writing–review & editing.

Conflicts of interest

There are no conflicts of interest to declare.

Acknowledgements

This work was financially supported by the National Natural Science Foundation of China (No. 51971002 and 52171197), Science Projects of Anhui Provincial Education Department (No. KJ2021A0393, 2022AH020033, 2022AH010025), Anhui Provincial Natural Science Foundation for Excellent Youth Scholars (No. 2108085Y16) and Gansu Provincial Science and Technology Major Projects (No. 21ZD8JA005).

Notes and references

1 L. Schlapbach and A. Züttel, *Nature*, 2001, **414**, 353–358.
2 R. Singh, M. Singh and S. Gautam, *Mater. Today: Proc.*, 2021, **46**(11), 5420–5427.
3 L. Ren, Y. H. Li, N. Zhang, Z. Li, X. Lin, W. Zhu, C. Lu, W. J. Ding and J. X. Zou, *Nano-Micro Lett.*, 2023, **15**(1), 93.
4 K. TMøller, T. R. Jensen, E. Akiba and H. W. Li, *Prog. Nat. Sci.*, 2017, **27**(1), 34–40.
5 N. A. A. Rusman and M. Dahari, *Int. J. Hydrogen Energy*, 2016, **41**(28), 12108–12126.
6 Q. Gao, G. Xia and X. Yu, *Nanoscale*, 2017, **9**(38), 14612–14619.
7 Z. Li, J. Z. Yu, Y. Zhang, D. M. Liu, C. Y. Wang, T. Z. Si, Y. T. Li and Q. A. Zhang, *J. Power Sources*, 2021, **491**, 229611.
8 Z. H. Ren, X. Zhang, Z. G. Huang, J. J. Hu, Y. Z. Li, S. Y. Zheng, M. X. Gao, H. G. Pan and Y. F. Liu, *Chem. Eng. J.*, 2022, **427**, 131546.
9 X. L. Ding, Y. T. Li, F. Fang, D. L. Sun and Q. A. Zhang, *J. Mater. Chem. A*, 2017, **5**(10), 5067–5076.
10 C. Peng, C. Z. Yang and Q. A. Zhang, *J. Mater. Chem. A*, 2022, **10**(23), 12409–12417.
11 T. Z. Si, F. H. Yin, X. X. Zhang, Q. A. Zhang, D. M. Liu and Y. T. Li, *Scr. Mater.*, 2023, **222**, 115052.
12 Z. K. Qin, L. Q. He, X. L. Ding, T. Z. Si, P. Cui, H. W. Li and Y. T. Li, *Inorganics*, 2023, **11**(5), 216.
13 J. A. Li, Y. R. Guo, X. J. Jiang, S. Lin and X. G. Li, *Renewable Energy*, 2020, **153**, 1140–1154.
14 B. Tu, H. Wang, Y. Wang, R. Li, L. Z. Ouyang and R. H. Tang, *Int. J. Hydrogen Energy*, 2022, **47**(33), 14952–14960.
15 W. F. Qiao, D. M. Yin, S. L. Zhao, N. Ding, L. Liang, C. L. Wang, L. M. Wang, M. He and Y. Cheng, *Chem. Eng. J.*, 2023, **465**, 142837.
16 F. Marques, M. Balcerzak, F. Winkelmann, G. Zepon and M. Felderhoff, *Energy Environ. Sci.*, 2021, **14**(10), 5191–5227.
17 E. P. George, D. Raabe and R. O. Ritchie, *Nat. Rev. Mater.*, 2019, **4**(8), 515–534.
18 S. Akrami, P. Edalati, M. Fuji and K. Edalati, *Mater. Sci. Eng., R*, 2021, **146**, 100644.
19 R. R. Shahi, A. K. Gupta and P. Kumari, *Int. J. Hydrogen Energy*, 2023, **48**(56), 21412–21428.
20 F. S. Yang, J. Wang, Y. Zhang, Z. Wu, Z. X. Zhang, F. Q. Zhao, J. Huot, J. G. Novaković and N. Novaković, *Int. J. Hydrogen Energy*, 2022, 11236–11249.
21 Y. F. Kao, S. K. Chen, J. H. Sheu, J. T. Lin, W. E. Lin, J. W. Yeh, S. J. Lin, T. H. Liou and C. W. Wang, *Int. J. Hydrogen Energy*, 2010, **35**(17), 9046–9059.
22 I. Kunce, M. Polański and T. Czujko, *Int. J. Hydrogen Energy*, 2017, **42**(44), 27154–27164.
23 P. Edalati, R. Floriano, A. Mohammadi, Y. T. Li, G. Zepon, H. W. Li and K. Edalati, *Scr. Mater.*, 2020, **178**, 387–390.
24 A. Mohammadi, Y. Ikeda, P. Edalati, M. Mito, B. Grabowski, H. W. Li and K. Edalati, *Acta Mater.*, 2022, **236**, 118117.
25 J. T. Chen, Z. Y. Li, H. X. Huang, Y. J. Lv, B. Liu, Y. T. Lin, Y. Wu, J. G. Yuan and Y. J. Wang, *Scr. Mater.*, 2022, **212**, 114548.
26 R. Floriano, G. Zepon, K. Edalati, G. L. B. G. Fontana, A. Mohammadi, Z. L. Ma, H. W. Li and R. J. Contieri, *Int. J. Hydrogen Energy*, 2020, **45**(58), 33759–33770.
27 R. Floriano, G. Zepon, K. Edalati, G. L. B. G. Fontana, A. Mohammadi, Z. L. Ma, H. W. Li and R. J. Contieri, *Int. J. Hydrogen Energy*, 2020, **45**(58), 33759–33770.
28 G. Andrade, G. Zepon, K. Edalati, A. Mohammadi, Z. L. Ma, H. W. Li and R. Floriano, *Int. J. Hydrogen Energy*, 2023, 34165–34182.
29 X. Ma, X. Ding, R. Chen, X. Gao, Y. Su and H. Cui, *RSC Adv.*, 2022, **12**(18), 11272–11281.
30 F. Izumi and T. Ikeda, A Rietveld-analysis program RIETAN-98 and its applications to zeolites, *Mater. Sci. Forum*, 2000, **198**, 321–324.
31 K. Manickam, D. M. Grant and G. S. Walker, *Int. J. Hydrogen Energy*, 2015, **40**(46), 16288–16296.
32 K. Manickam, D. M. Grant and G. S. Walker, *Int. J. Hydrogen Energy*, 2015, **40**(46), 16288–16296.
33 N. Yurchenk, N. Stepanov and G. Salishchev, *Mater. Sci. Technol.*, 2017, **33**(1), 17–22.
34 M. M. Nygård, G. Ek, D. Karlsson, M. H. Sørby and M. Sahlberget, *Acta Mater.*, 2019, **175**, 121–129.
35 H. Pang, Z. Li, C. Zhou, H. Wang and L. Z. Ouyang, *Int. J. Hydrogen Energy*, 2018, **43**(31), 14541–14549.
36 H. Wagner, S. Ott, K. Jurcic, J. Morton and A. Neszmelyi, *Planta Med.*, 1983, **48**(07), 136–141.
37 Z. M. Li, H. Wang, L. Z. Ouyang, J. W. Liu and M. Zhu, *J. Alloys Compd.*, 2017, **704**, 491–498.

Open Access Article. Published on 19 de juliol 2023. Downloaded on 31/1/2026 14:14:17.
This article is licensed under a Creative Commons Attribution-NonCommercial 3.0 Unported Licence.

38 Y. L. Zhang, J. S. Li, T. B. Zhang, H. C. Kou, R. Hu and X. Y. Xue, *Int. J. Hydrogen Energy*, 2014, **39**(34), 19637–19645.
39 X. F. Ma, X. Ding, R. Chen, X. G. Chan, Q. Song and H. Z. Cui, *Intermetallics*, 2023, **157**, 107885.
40 K. R. Cardoso, V. Roche, Jr, A. M. Jorge, F. J. Antiqueira, G. Zepon and Y. Champion, *J. Alloys Compd.*, 2021, **858**, 158357.
41 R. B. Strozi, D. R. Leiva, J. Huot, W. J. Botta and G. Zepon, *Int. J. Hydrogen Energy*, 2021, **46**(50), 25555–25561.

© 2023 The Author(s). Published by the Royal Society of Chemistry